Available online at www.sciencedirect.com
SCIENCE DIRECT®
Journal of Colloid and Interface Science 269 (2004) 192–204
JOURNAL OF Colloid and Interface Science
www.elsevier.com/locate/jcis

A method for determining electrophoretic and electroosmotic mobilities using AC and DC electric field particle displacements

M.H. Oddy * and J.G. Santiago

Department of Mechanical Engineering, Stanford University, Stanford, CA 94305, USA

Received 19 March 2003; accepted 4 June 2003

Abstract

We have developed a method for measuring the electrophoretic mobility of submicrometer, fluorescently labeled particles and the electroosmotic mobility of a microchannel. We derive explicit expressions for the unknown electrophoretic and the electroosmotic mobilities as a function of particle displacements resulting from alternating current (AC) and direct current (DC) applied electric fields. Images of particle displacements are captured using an epifluorescent microscope and a CCD camera. A custom image-processing code was developed to determine image streak lengths associated with AC measurements, and a custom particle tracking velocimetry (PTV) code was devised to determine DC particle displacements. Statistical analysis was applied to relate mobility estimates to measured particle displacement distributions.

Keywords: Electroosmosis; Electrophoresis; Mobility measurement; Zeta potential

1. Introduction

Electroosmosis and electrophoresis are key transport processes used in a variety of bioanalytical applications including capillary electrophoresis, isoelectric focusing, and capillary electrochromatography [1]. Electroosmosis is the bulk motion of liquid over a stationary, charged surface in response to an applied electric field [2]. Electrophoresis is the drift velocity of a charged species relative to a background medium due to the application of an electric field. The electrophoretic mobility of a particle or molecule, μ_{ep}, is defined as the proportionality factor between the electrophoretic particle velocity, $\boldsymbol{u}_{\mathrm{ep}}$, and the local electric field, $\boldsymbol{E}$: $\boldsymbol{u}_{\mathrm{ep}} = \mu_{\mathrm{ep}}\boldsymbol{E}$. Similarly, the steady state electroosmotic flow velocity, $\boldsymbol{u}_{\mathrm{eo}}$, defined as the fluid velocity at the interface between the bulk neutral liquid and an electrical double layer on the wall of a liquid channel, can be expressed in terms of an electroosmotic mobility, μ_{eo}, as $\boldsymbol{u}_{\mathrm{eo}} = \mu_{\mathrm{eo}}\boldsymbol{E}$ [3]. Electrophoretic mobility holds particular importance in chemical and biochemical separations [1].

In addition to basic colloid and separation science applications, knowledge of a tracer particle's electrophoretic mobility is also important in the application of optical velocimetry techniques such as micro particle image velocimetry (μ-PIV) to the quantification of electrokinetic velocity fields [4,5]. Current techniques for measuring electrophoretic mobility include an electroacoustic method [6], electrophoretic light scattering [7], and AC/DC microelectrophoresis [8,9]. Electroacoustic (EA) methods such as electrokinetic sonic amplitude determine both particle size and electrophoretic mobility by measuring the acoustic pressure generated by particles in a suspension and responding to a high-frequency electric field (frequencies of order 1 MHz are used) [6]. EA methods require that test particles have a density different from that of the suspending medium [10]. Electrophoretic light scattering [7] measures the Doppler shift of optical backscatter from particles. Particle-to-particle variance in the light-scattering properties, however, is a potential drawback of this method, as well as the fact that single-particle-specific information is difficult to obtain. A static and uniform electric field is used in DC microelectrophoresis to electrophoretically advect particles within a closed test cell usually composed of a long thin capillary with sealed ends. Particle displacements are measured optically at the so-called stationary level or Komagata plane [11], which forms within this closed-cell flow field. The accuracy of this method relies on an accurate knowledge of the stationary plane location, which is a strong function of cell geometry. DC microelectrophoresis measurements can be difficult due

* Corresponding author.
E-mail address: oddy@stanford.edu (M.H. Oddy).

0021-9797/$ – see front matter
doi:10.1016/S0021-9797(03)00601-5

to electrode polarization and the introduction of unwanted gas bubbles resulting from electrolysis [8]. The latter problems with bubbles may be partially mitigated in conventional AC microelectrophoresis, where low-frequency (<100 Hz) alternating fields are applied to suspensions in closed cells. Particle oscillation amplitudes are recorded at the Komagata planes and related to the electrophoretic mobility [8]. Both DC and AC microelectrophoresis are particle-tracking techniques and typically require a sufficiently dilute concentration of the colloidal solution so that individual particles are readily discernible by the detector.

Knowledge of the electroosmotic mobility of microchannels is critical to the optimization of capillary electrophoresis measurements [1] and to the design of electrokinetic microfluidic devices [4,12]. Traditional, "workhorse" methods of quantifying electroosmotic mobility include streaming potential and current monitoring. In streaming potential, a known pressure gradient is applied to a capillary and the mean capillary zeta potential is estimated by measurement of the resulting electric potential along the capillary axis [2]. An analogous method is streaming current, in which the ends of the capillary are grounded and the advection of charge in the electrical double layers causes a measurable current flow. In both cases, zeta potential is related to μ_{eo} using electrokinetic flow theory [13]. Current monitoring, first demonstrated by Huang et al. [14], relies on measurement of the time-dependent decrease of the ionic current through a channel as an electrolyte of a lower conductivity displaces a higher conductivity solution.

In this paper, we present a method for quantifying electrophoretic and electroosmotic mobilities, which combines elements of both DC and AC microelectrophoresis. The method is applied to a channel connected to reservoirs that are open to the atmosphere (allowing for the escape of electrolysis gases). The method uses a high-resolution imaging system combined with a super-resolved particle tracking velocimetry (PTV) technique and a streak-processing algorithm to quantify distributions of particle displacements acquired under both DC and AC field conditions. Use of both DC and AC information eliminates the need for measuring particle displacements at stationary plane/surface in the microchannel. The method also enables the individual quantification of a relatively large number of particles in a solution. The technique allows more than 1000 particles to be quantified in a single experiment.

2. Theory of mobility measurement through DC and AC displacements

In this section we derive equations describing the displacement of a particle suspended in channel filled with an electrolyte and subjected to either a DC or an AC electric field. These equations are combined to yield explicit relationships for the electrophoretic and electroosmotic mobilities of an ensemble of particles. Both mobilities are found to be a function of the measured DC and AC particle displacements, as well as magnitude and phase of the local fluid velocity. We begin by considering particle dynamics.

2.1. Equations of particle motion

A charged particle suspended in a liquid medium subjected to an electric field will experience forces resulting from Coulombic interaction, viscous drag, polarization, inertia, and random thermal motion. The particle is here assumed to have a specific gravity of unity, and hence a negligible buoyancy force. For simplicity, we also neglect Brownian motion since Brownian displacements are small compared to electrophoretic displacements for the time scales of interest. In a laboratory frame of reference, the velocity of the particle at any time is a linear superposition of the electrophoretic velocity and local fluid velocity arising from electroosmosis:

$$\boldsymbol{u}_p = \boldsymbol{u}_{\text{ep}} + \boldsymbol{u}_{\text{fl}}. \tag{1}$$

Before the forms of the electrophoretic and local fluid velocity terms are determined, it is helpful to consider charge relaxation processes and their associated time scales. Of particular interest is the transient motion of a charged colloidal particle and its ionic cloud when subjected to a sudden change of electric field. The relevant relaxation processes for the present study, listed in order of increasing time scale, are the inertial response of the particle, the polarization of the particle's double layer, the polarization of the electrolyte in the region near the particle, and the viscous diffusion of momentum within the bulk fluid [15–17]. The inertial response time τ_p of the particle may be estimated to be of order $O(a^2\rho_p/\eta)$, where a is the particle radius, ρ_p is the particle density, and η is the absolute viscosity of the surrounding liquid [18]. For the 500-nm-diameter particles used in this study, the inertial response time $\tau_p = O(10^{-7})$ s. For a symmetric electrolyte, the time scale for double layer polarization may be estimated as $\tau_{\text{dl}} = O(\lambda_D^2/D)$, where λ_D is the Debye length and D the diffusion coefficient of the ions [15]. Similarly, the time scale associated with the polarization of the net-neutral regions of the concentration field near the particle (outside of the particle electrical double layer), otherwise known as concentration polarization, may be estimated as $\tau_{\text{cp}} = O(a^2/D)$ [16,19]. For the present solution $\tau_{\text{dl}} = O(10^{-5})$ s and $\tau_{\text{cp}} = O(10^{-5})$ s. Last, the time for the electroosmotic velocity profile to become steady may be estimated from $\tau_{\text{eo}} = O(D_h^2\rho/\eta)$, where D_h is the hydraulic diameter of the electroosmotic channel and ρ is the density of the bulk fluid. For our microchannel $\tau_{\text{eo}} = O(10^{-1})$ s.

The various time scales above may be compared to the characteristic time scale of the electric forcing function used in our study. The shortest AC field period of interest here, $\tau_{\text{AC}} = 2\pi/\omega$, is $O(10^{-2})$ s, where ω is the applied angular frequency. Since $\tau \gg \tau_p$ we expect that transients associated with the inertial response of the particle are not observable. Also, since $\tau \gg \tau_{\text{dl}}$ and $\tau \gg \tau_{\text{cp}}$, we expect that the particle will respond faithfully to the alternating electric field

with a mobility equal to that of the static electric field condition [15]. This time-scale analysis indicates that the electrophoretic drift component of the particle's motion should be in phase with the alternating electric field. Finally, provided that particles are observed at times greater than τ_{eo}, from the initial application of the electric field, the local fluid velocity will be steady. Hence, we conclude that the expression $\boldsymbol{u}_{ep} = \mu_{ep}\boldsymbol{E}$ can be used, where $\boldsymbol{E}$ is either the static $\boldsymbol{E}_{DC}$ or alternating $|\boldsymbol{E}_{AC}|\exp(i\omega t)$ electric fields for the frequencies of interest.

2.2. Oscillatory electroosmotic velocity field (one- and two-dimensional)

We here present a derivation of the oscillatory electroosmotic velocity field in an open-ended rectangular-cross-section microchannel with an applied axial field. Consider the microchannel shown in Fig. 1, where the channel walls are composed of a dielectric material. Here the axial dimension (x-direction) is much larger than either the spanwise (y-direction) or transverse (z-direction) dimension (i.e., $w/L \ll 1$ and $d/L \ll 1$). As discussed in Section 3 below, the microchannel has spanwise and transverse length scales of 2.0 mm and 200 μm, respectively, and contains a low-conductivity solution (e.g., 10 μS/cm) to minimize temperature gradients that may arise due to Joule heating by order 20 V_{rms}/mm electric fields. The bulk fluid properties are considered to be homogeneous in an isothermal system.

We also assume that the thickness of the electric double layer (EDL), characterized by the Debye length [20] of the electrolyte, is small relative to the transverse and spanwise dimensions, w and d, respectively. The application of an electric field imparts an electric body force on the ions contained within the thin EDL. Viscous drag associated with ion movement within the EDL sets into motion the bulk liquid.

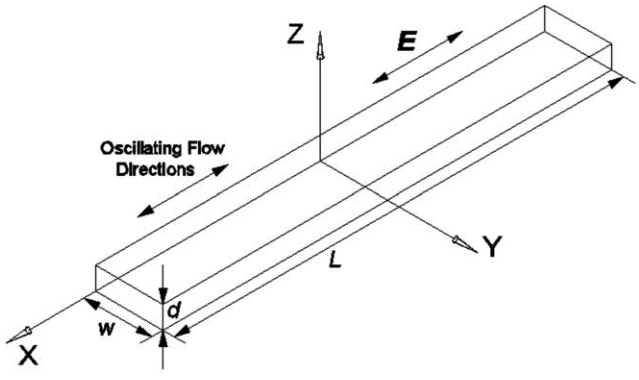

Fig. 1. Schematic of the flow domain showing a rectangular cross-section microchannel and coordinate system. Axial, transverse, and spanwise directions are given by x, y, and z, respectively. The channel has a width w and depth d. For the two-dimensional solution in Appendix A, the slip velocity is assumed to be axially constant, yet differs on each wall. The one-dimensional solution provided in this section is valid for high-aspect ratio ($w/d \gg 1$) microchannels having equal electroosmotic mobility on both the top and bottom walls (at $z = 0$ and d). Parallel flow with uniform pressure is assumed.

With the isothermal and thin EDL assumptions, the bulk may be considered to be effectively net-neutral. For $w/L \ll 1$ and $d/L \ll 1$, the flow field may be safely assumed to be parallel. The uniform cross-section of this microchannel and the low particle densities of interest allows the dielectrophoretic body force arising from nonuniform electric fields to be neglected. As the channel's zeta potential is also assumed to be uniform in the axial direction, pressure gradients along the axis of the microchannel are not generated by electroosmotic flow. Under these assumptions and conditions, the x-momentum equation for this low Reynolds number, parallel flow (i.e., $\boldsymbol{u} = [u(y,z,t), 0, 0]$) reduces to

$$\rho\frac{\partial u}{\partial t} = \eta\left(\frac{\partial^2 u}{\partial y^2} + \frac{\partial^2 u}{\partial z^2}\right), \tag{2}$$

where u is the axial fluid velocity, ρ the fluid density, and η the absolute viscosity. Oddy and Santiago [21] have shown experimentally that the parallel flow assumption may not be valid in this flow field for electric field strengths approaching 100 V/mm. Above this approximate critical field value, the flow exhibits an instability, which results in strong fluctuating transverse velocity components and which is currently under study.

The steady fluid flow of electrokinetic microflows having a λ_D that is much smaller than any cross-sectional dimension are well modeled with a slip velocity boundary condition at the wall of the form

$$\boldsymbol{U}_{slip,j} = \mu_{eo,j}\boldsymbol{E}, \tag{3}$$

where μ_{eo} denotes the electroosmotic mobility and $\boldsymbol{E}$ represents the local electric field. The solution to Eq. (2) subject to Eq. (3) is a trivial plug flow solution of uniform velocity of the form $\mu_{eo}\boldsymbol{E}$. For the remainder of the paper, we shall assume $\boldsymbol{E}_{DC} = [E_{DC}, 0, 0]$ and $\boldsymbol{E}_{AC} = [E_{AC}, 0, 0]$, since the applied potential difference is in the axial direction. The application of a harmonically oscillating electric field *forces* the EDL to oscillate sinusoidally with the frequency ω of the applied field. For applied frequencies less than approximately 1 MHz and a thin EDL (where $\lambda_D/w \ll 1$ and $\lambda_D/d \ll 1$), the slip velocity boundary condition is again valid [22], and can be expressed as

$$U_{slip,j} = \mu_{eo,j}|E_{AC}|\cos(\omega t), \tag{4}$$

where $|E_{AC}|$ is the peak-to-peak amplitude of the applied electric field. Equations (3) and (4) are for the general case where each of the four channel walls $j = 1$ through 4 may have differing electroosmotic mobilities.

The unsteady two-dimensional (2-D) solution of Eq. (2), subject to Eq. (4), is given in Appendix A. This full 2-D solution is provided for researchers wishing to adapt the mobility measurement technique described here to microchannels having smaller aspect ratios and/or walls with azimuthally varying electroosmotic mobility (e.g., as in the case of polydimethylsiloxane substrate microchannels with a glass coverslip). Since the microchannel used in this study has $w/d = 10$, we will discuss here only the one-dimensional (1-D)

solution $\boldsymbol{u} = [u(z,t), 0, 0]$ valid for high-aspect-ratio microchannels. Moreover, since the microchannel consisted of a glass capillary with uniform surface properties on all four walls, the following analysis assumes the zeta-potential is equal and spatially-invariant on all the four walls.

For large aspect ratio (AR) capillaries (i.e., $\mathrm{AR} = w/d \gg 1$), the velocity profile along the section $u(w/2, z, t)$ may be approximated with a one-dimensional profile $u(z,t)$. Oddy and Santiago [21] give the 1-D, steady, time-periodic electroosmotic flow field as

$$u_{\mathrm{eof,AC}}(\tilde{z},\tilde{t}) = Re\big\{\big|\hat{u}(\tilde{z})\big|\exp\big[i\gamma(\tilde{z})\big]\mu_{\mathrm{eo}}|E_{\mathrm{AC}}|\exp(i\tilde{t})\big\}, \quad (5)$$

where $|\hat{u}(\tilde{z})| \in [0,1]$ and $\gamma(\tilde{z})$ is the coordinate dependent phase of the complex-valued $\hat{u}(\tilde{z})$. $\tilde{z}$ and $\tilde{t}$ are nondimensional spatial and temporal variables defined as z/d and ωt, respectively. Here the following boundary conditions were applied: $U_{\mathrm{slip},1} = U_{\mathrm{slip},2} = \mu_{\mathrm{eo}}|E_{\mathrm{AC}}|\cos(\omega t)$. This solution is essentially an application of Stokes's second problem in a bounded domain (i.e., between two flat plates of infinite extent). $\hat{u}(\tilde{z})$ is given by

$$\hat{u}(\tilde{z}) = \frac{\sinh[\beta(1+i)(1-\tilde{z})] + \sinh[\beta(1+i)\tilde{z}]}{\sinh[\beta(1+i)]}, \quad (6)$$

where $\beta = d/\delta$ and the penetration depth δ is defined as $(2\eta/\rho\omega)^{0.5}$. Figure 2a compares the magnitude of the 1- and 2-D solutions for $|u_{\mathrm{eo,AC}}|$ nondimensionalized by the slip velocity amplitude $\mu_{\mathrm{eo}}|E_{\mathrm{AC}}|$. Figure 2b plots the phase γ of the complex-valued $u_{\mathrm{eo,AC}}$. Both $|u_{\mathrm{eo,AC}}|$ and γ are plotted for varying AR as a function of β, and computed for the dimensionless spanwise and transverse centerline coordinate $\tilde{y} = \tilde{z} = 0.5$ (the center location of our measurement volume). A comparison between the 1- and 2-D solutions shows that for $\mathrm{AR} \geqslant 3$ and $\beta \in [0,4]$ the error incurred in estimating the velocity at the microchannel centerline with the 1-D solution is less than 2%. The error is less than 3% when for $0.4 \leqslant \tilde{y} \leqslant 0.6$ and $\mathrm{AR} \geqslant 3$. Having derived expressions for the fluid velocity fields under both AC and DC conditions, we now turn to deriving equations characterizing particle displacement.

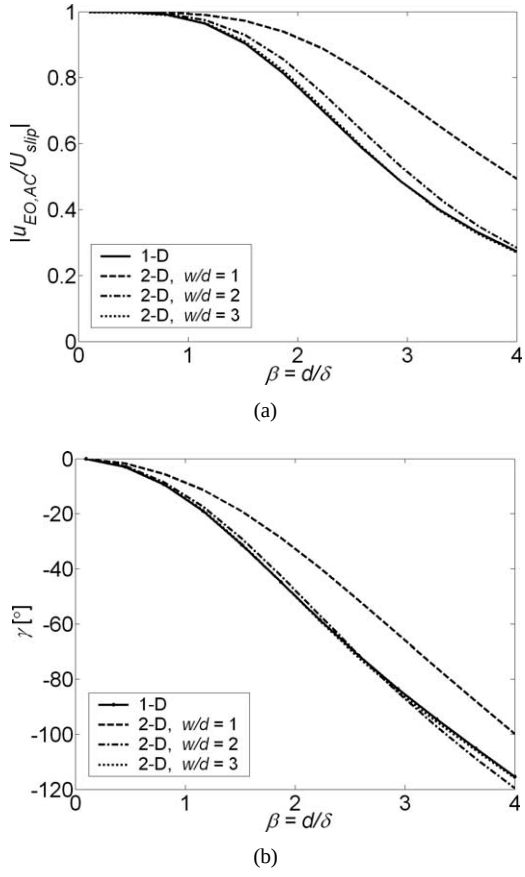

Fig. 2. Comparison between one- and two-dimensional flow solutions for a time-periodic, electroosmotic velocity profile in a microchannel with planar walls as a function of the parameter $\beta = d/\delta$. Both plots are for the spanwise and transverse centerline of the microchannel ($\tilde{y} = \tilde{z} = 0.5$). The 1-D estimate for the velocity converges to the 2-D solution for increasing aspect ratio. In the range $\beta \in [0,4]$, the difference between the 1-D and 2-D solutions is less than 2% for $\mathrm{AR} \geqslant 3$.

2.3. AC particle displacement equation

For a harmonically oscillating electric field, the electroosmotic and electrophoretic velocities are, respectively:

$$u_{\mathrm{eo,AC}} = Re\big\{|\hat{u}|\exp(i\gamma)\mu_{\mathrm{eo}}|E_{\mathrm{AC}}|\exp(i\omega t)\big\}, \quad (7)$$

$$u_{\mathrm{ep,AC}} = Re\big\{\mu_{\mathrm{ep}}|E_{\mathrm{AC}}|\exp(i\omega t)\big\}. \quad (8)$$

Both velocity components are parallel with the applied electric field. Note that μ_{eo} and μ_{ep} are real-valued constants that represent the electroosmotic and electrophoretic mobilities, respectively. Both μ_{eo} and μ_{ep} are assumed to be independent of the applied frequency for the relatively low frequencies considered here. This assumption should be valid for frequencies less than 10 kHz, provided the following conditions are met: $\rho_p/\rho \leqslant 4$ and $a/\lambda_D \geqslant 0.1$ [6].

Substituting Eqs. (7) and (8) into Eq. (1), the time-dependent velocity of a particle subject to an AC field is

$$u_{\mathrm{AC}} = |\hat{u}|\mu_{\mathrm{eo}}|E_{\mathrm{AC}}|\cos(\omega t + \gamma) + \mu_{\mathrm{ep}}|E_{\mathrm{AC}}|\cos(\omega t). \quad (9)$$

Integrating the expression for the AC velocity, we obtain the AC displacement,

$$x_{\mathrm{AC}} = -\frac{1}{\omega}\big[|\hat{u}|\mu_{\mathrm{eo}}|E_{\mathrm{AC}}|\sin(\omega t + \gamma) + \mu_{\mathrm{ep}}|E_{\mathrm{AC}}|\sin(\omega t)\big] + C_1, \quad (10)$$

where the constant C_1 determines the center of the trajectory. Recognizing this as the sum of two harmonics of equal frequency, the AC displacement becomes

$$x_{\mathrm{AC}} = -\frac{|E_{\mathrm{AC}}|}{\omega}\sqrt{\hat{u}\hat{u}^*\mu_{\mathrm{eo}}^2 + \mu_{\mathrm{ep}}^2 + 2|\hat{u}|\cos(\gamma)\mu_{\mathrm{eo}}\mu_{\mathrm{ep}}} \times \sin(\omega t + \phi) + C_1, \quad (11)$$

where the asterisk represents the complex conjugate. As we will discuss below, our method requires only the peak-to-peak amplitude of the particle displacement, therefore we

only consider the amplitude. The final expression for the amplitude of the peak-to-peak AC displacement becomes

$$d_{\mathrm{AC}} = \frac{2|E_{\mathrm{AC}}|}{\omega}\sqrt{\hat{u}\hat{u}^*\mu_{\mathrm{eo}}^2 + \mu_{\mathrm{ep}}^2 + 2|\hat{u}|\cos(\gamma)\mu_{\mathrm{eo}}\mu_{\mathrm{ep}}}, \quad (12)$$

where d_{AC} is by definition a positive quantity.

2.4. DC particle displacement equation

The derivation of the DC particle displacement equation is much simpler than the AC counterpart. For a static DC electric field the electroosmotic and electrophoretic velocities are

$$u_{\mathrm{eo,DC}} = \mu_{\mathrm{eo}} E_{\mathrm{DC}}, \quad (13)$$

$$u_{\mathrm{ep,DC}} = \mu_{\mathrm{ep}} E_{\mathrm{DC}}. \quad (14)$$

Both velocity components are parallel and in the direction of the applied electric field. Both μ_{eo} and μ_{ep} are real-valued and identical in magnitude and sign to the respective electroosmotic and electrophoretic mobility used in the AC equations above. Substituting Eqs. (13) and (14) into Eq. (1), the DC particle velocity is

$$u_{\mathrm{DC}} = (\mu_{\mathrm{eo}} + \mu_{\mathrm{ep}})E_{\mathrm{DC}}. \quad (15)$$

Signs of the mobilities and the DC electric field determine the sign of the particle velocity. Integrating for a finite time Δt, we arrive at an expression for the DC displacement,

$$x_{\mathrm{DC}} = (\mu_{\mathrm{eo}} + \mu_{\mathrm{ep}})E_{\mathrm{DC}}\Delta t + C_2, \quad (16)$$

where the constant C_2 determines the initial location of the particle.

2.5. Theoretical electrophoretic mobility determination

We can now manipulate the expressions for the DC and AC particle displacements to derive relations for unknown mobilities μ_{ep} and μ_{eo}. Combining Eqs. (12) and (16), two quadratic equations containing either μ_{ep} or μ_{eo} are obtained by eliminating either μ_{eo} or μ_{ep}, respectively:

$$\begin{aligned} 0 = {} & \big[\hat{u}\hat{u}^* - 2|\hat{u}|\cos(\gamma) + 1\big]\mu_{\mathrm{ep}}^2 \\ & + 2\mu_{\mathrm{DC}}\big[|\hat{u}|\cos(\gamma) - \hat{u}\hat{u}^*\big]\mu_{\mathrm{ep}} \\ & + \hat{u}\hat{u}^*\mu_{\mathrm{DC}}^2 - \mu_{\mathrm{AC}}^2, \end{aligned} \quad (17)$$

$$\begin{aligned} 0 = {} & \big[\hat{u}\hat{u}^* - 2|\hat{u}|\cos(\gamma) + 1\big]\mu_{\mathrm{eo}}^2 \\ & + 2\mu_{\mathrm{DC}}\big[|\hat{u}|\cos(\gamma) - 1\big]\mu_{\mathrm{eo}} \\ & + \mu_{\mathrm{DC}}^2 - \mu_{\mathrm{AC}}^2. \end{aligned} \quad (18)$$

Here we have defined the variables

$$\mu_{\mathrm{DC}} = \frac{x_{\mathrm{DC}}}{E_{\mathrm{DC}}\Delta t}, \quad (19)$$

$$\mu_{\mathrm{AC}} = \frac{\omega d_{\mathrm{AC}}}{2|E_{\mathrm{AC}}|}, \quad (20)$$

which have units of mobility [$\mathrm{m}^2/\mathrm{V\,s}$]. Equations (17) and (18) reveal the functional dependence of μ_{ep} and μ_{eo}, namely $\mu_{\mathrm{ep}} = \mu_{\mathrm{ep}}(\hat{u}, \gamma, \mu_{\mathrm{DC}}, \mu_{\mathrm{AC}})$ and $\mu_{\mathrm{eof}} = \mu_{\mathrm{eof}}(\hat{u}, \gamma, \mu_{\mathrm{DC}}, \mu_{\mathrm{AC}})$. Equations (17) and (18) may be written succinctly as

$$0 = \mu_{\mathrm{ep}}^2 P + \mu_{\mathrm{ep}} Q + R, \quad (21)$$

$$0 = \mu_{\mathrm{eof}}^2 P + \mu_{\mathrm{eof}} S + T, \quad (22)$$

where

$$\begin{aligned} P &= \big(\hat{u}\hat{u}^* - 2|\hat{u}|\cos(\gamma) + 1\big), \\ Q &= 2\mu_{\mathrm{DC}}\big(|\hat{u}|\cos(\gamma) - \hat{u}\hat{u}^*\big), \\ R &= \hat{u}\hat{u}^*\mu_{\mathrm{DC}}^2 - \mu_{\mathrm{AC}}^2, \\ S &= 2\mu_{\mathrm{DC}}\big(|\hat{u}|\cos(\gamma) - 1\big), \\ T &= \mu_{\mathrm{DC}}^2 - \mu_{\mathrm{AC}}^2. \end{aligned} \quad (23)$$

Hence the solution for the electrophoretic mobility is

$$\mu_{\mathrm{ep}} = \frac{-Q \pm \sqrt{Q^2 - 4PR}}{2P} \quad (24)$$

and the electroosmotic mobility is

$$\mu_{\mathrm{eo}} = \frac{-S \pm \sqrt{S^2 - 4PT}}{2P}. \quad (25)$$

The solutions given by Eqs. (24) and (25) are plotted in Fig. 3 as a function of μ_{DC} and μ_{AC} for $\beta = 2$ and $z = 0.5$ (channel centerline). The solutions for μ_{ep} and μ_{eo} are naturally restricted to real values.

As shown by the multiple roots of the solution (see Eqs. (24) and (25)), the amplitude-of-AC-displacement method described here requires additional information to determine the sign of the electrophoretic particle mobility. This ambiguity is a direct result of discarding phase information in the measurement by using only the peak-to-peak amplitude of the AC displacement (a methodology which facilitates experiments). However, the technique as described here can be used to determine both the particle and electroosmotic mobilities, if the sign of either mobility is known. Once the sign of one mobility is known, the sign of the other mobility can be determined from Fig. 3 and the condition that

$$\mu_{\mathrm{DC}} = \mu_{\mathrm{eo}} + \mu_{\mathrm{ep}}. \quad (26)$$

The sign of the mobility of a surface can often be determined from a known value of the surface's isoelectric point (pI), which is the pH at which the surface zeta potential is zero. For example, for silica and borosilicate glass surfaces in contact with aqueous solutions with pH above about 2.3 [23], the surface charge is expected to be determined largely from the deprotonation of silanol groups, which results in a positive electroosmotic mobility (associated with a negative surface charge). For example, Hunter discusses in detail the isoelectric point characteristic of several material surfaces including aluminum oxide and titanium oxide in Chapter 6 of his book. For the infrequent cases where neither the sign of the particle nor that of the wall of a system is known, various methods can be employed to first determine the sign of the wall mobility, including current monitoring or the weighing method [24].

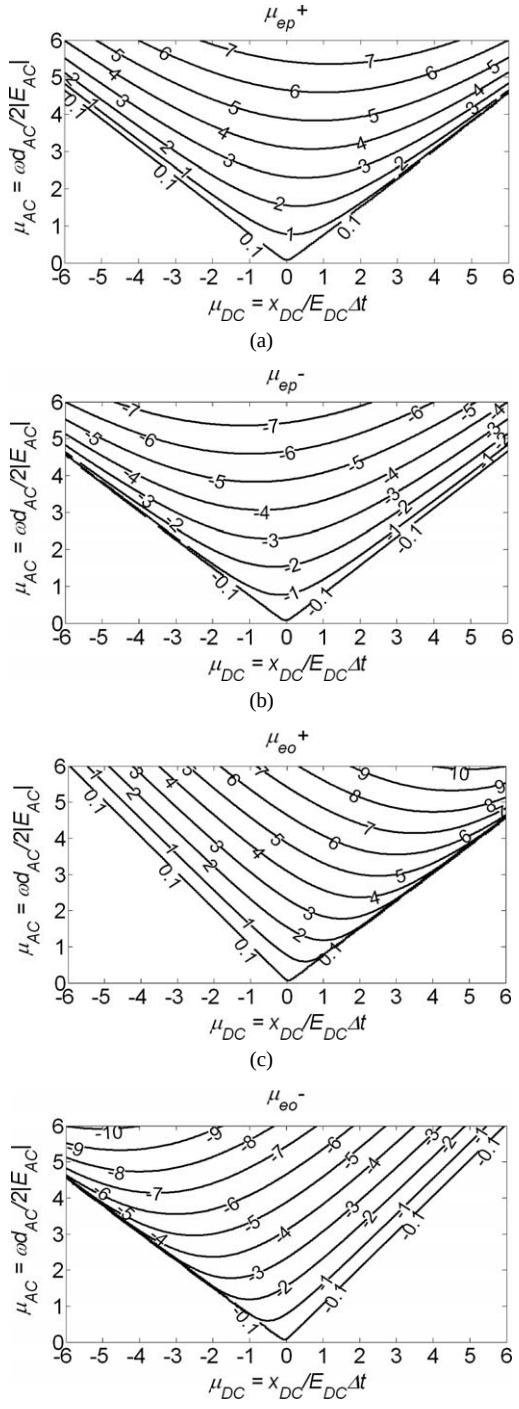

Fig. 3. Contour maps of μ_{ep} plotted as a function of μ_{DC} and μ_{AC} for $\beta = 2$ and $\tilde{z} = 0.5$ (channel centerline). The following four conditions are plotted: a solution with a positive root of μ_{ep} (a), a negative root of μ_{ep} (b), a positive root of μ_{eo} (c), and a negative root of μ_{eo} (d).

2.6. Distribution statistics

In our technique, we measure μ_{DC} and μ_{AC} for different, representative particle ensembles from the same batch of particles. Both μ_{DC} and μ_{AC} are not known for any one particle. Therefore, before the electrophoretic and electroosmotic mobilities may be determined, a statistical method is required to relate distributions of μ_{DC} and μ_{AC} to distributions of μ_{ep} and μ_{eo} using Eqs. (24) and (25). This statistical method is described below.

Since the methods for calculating the distributions of μ_{ep} and μ_{eo} are very similar, we provide a detailed derivation here only for the electrophoretic mobility distribution and then provide both results. We begin with the functional relationship between μ_{ep}, μ_{DC}, and μ_{AC},

$$\mu_{ep} = g(\mu_{DC}, \mu_{AC}), \tag{27}$$

as given by Eq. (24). We may determine the probability density function (PDF) of μ_{ep}, $f_{\mu_{ep}}$, by first computing the cumulative distribution function (CDF) of μ_{ep}, $F_{\mu_{ep}}$ (defined as the probability that μ_{ep} is less than some value μ'_{ep}):

$$F_{\mu_{ep}} = \iint\limits_{g(\mu_{DC},\mu_{AC})\leqslant\mu_{ep}} f_{\mu_{DC}\mu_{AC}}\, d\mu'_{DC}\, d\mu'_{AC}. \tag{28}$$

Variables with an apostrophe represent arbitrary elements in the range of the associated variable, and $f_{\mu_{DC}\mu_{AC}}$ is the joint probability density function of μ_{DC} and μ_{AC}. Equation (28) is further simplified by assuming that the probability densities of μ_{DC} and μ_{AC} are independent. This assumption is justified as the measurements of μ_{DC} and μ_{AC} are uncorrelated, since both the DC and AC displacement measurements were made on two distinct, yet representative sample populations. Therefore, μ_{AC} is unaffected by conditioning on the value of μ_{DC} and vice versa. Consequently, the joint probability density function may be written as

$$f_{\mu_{DC}\mu_{AC}} = f_{\mu_{DC}} f_{\mu_{AC}}. \tag{29}$$

Equation (28) now becomes

$$F_{\mu_{ep}} = \iint\limits_{g(\mu_{DC},\mu_{AC})\leqslant\mu_{ep}} f_{\mu_{DC}} f_{\mu_{AC}}\, d\mu'_{DC}\, d\mu'_{AC}. \tag{30}$$

Finally, the PDF of μ_{ep} is derived by differentiating the CDF of μ_{ep} with respect to μ_{ep} or

$$f_{\mu_{ep}} = \frac{d}{d\mu_{ep}}\left[F_{\mu_{ep}}\right]. \tag{31}$$

When Eq. (30) is substituted into Eq. (31), the distribution for μ_{ep} becomes

$$f_{\mu_{ep}} = \frac{d}{d\mu_{ep}}\left(\iint\limits_{\frac{-Q\pm\sqrt{Q^2-4PR}}{2P}\leqslant\mu'_{ep}} f_{\mu_{DC}} f_{\mu_{AC}}\, d\mu'_{DC}\, d\mu'_{AC} \right). \tag{32}$$

Using the above methodology, the distribution or variation in μ_{eo} may be written as

$$f_{\mu_{eo}} = \frac{d}{d\mu_{eo}}\left(\iint\limits_{\frac{-S\pm\sqrt{S^2-4PT}}{2P}\leqslant\mu'_{eo}} f_{\mu_{DC}} f_{\mu_{AC}}\, d\mu'_{DC}\, d\mu'_{AC} \right). \tag{33}$$

In both cases, the width of the mobility distribution estimates, $f_{\mu_{ep}}$ and $f_{\mu_{eo}}$, are determined by the underlying particle-to-particle variability in mobility as well as the uncertainty in the measurement of particle displacements; both of which contribute to $f_{\mu_{DC}}$ and $f_{\mu_{AC}}$.

3. Experimental apparatus and method

3.1. Measurement cell

A schematic of the measurement cell is shown in Fig. 4. The cell consists of a borosilicate glass capillary (Wilmad Labglass, Buena, NJ) with a rectangular cross-section of 2.0 mm × 200 μm inner dimensions (ID) and a length of 40 mm. Fluorescent polystyrene spheres of diameter 490 nm (Interfacial Dynamics Corp., Portland, OR) with a specific gravity of 1.05 were used. Prior to loading the measurement cell with the particle suspension, a 100 mM sodium hydroxide solution (1.6 ml at 80 μl/min) was flushed through the capillary to prepare the surface for electroosmotic flow experiments. The NaOH was then flushed from the capillary with deionized water (1.6 ml at 40 μl/min). In all of the experiments described here, deionized water was the background electrolyte. Prior to seeding, the electrical conductivity and pH of the deionized water were recorded. The electrical conductivity was measured using a conductivity meter (CON 500, Oakton Instruments, Vernon Hills, IL) to be 3.0 μS/cm, and the pH was 7. The particle seeding density of the suspension was approximately 3.1×10^8 particles/ml.

DC and AC electric fields were applied using platinum electrodes inserted into 130-μl reservoirs at the ends of the microchannel cell, as shown in Fig. 4. For the DC measurements, a high-voltage power supply (677b, Trek, Inc., Medina, NY) was used to apply 50 V to the high-voltage electrode. For the AC measurements, a function generator (Agilent, 33120a) coupled to a high-voltage (0 to ±10 kV maximum) amplifier (10/10b, Trek, Inc., Medina, NY) was used to apply a sinusoidally varying potential with peak-to-peak voltages of ±1000 V and a frequency of 30 Hz.

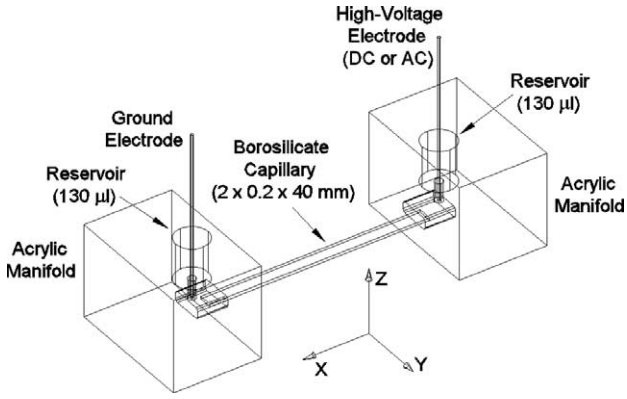

Fig. 4. Schematic of the test measurement cell. A borosilicate capillary with a rectangular cross-section (2 × 0.2 mm ID) and a length of 40 mm is sealed to acrylic manifolds at either end using silicone adhesive. A liquid path extending from the inlet acrylic manifold through the capillary and out through the outlet acrylic manifold completes the electric circuit. Fluid enters and exits the capillary through the 130-μl reservoirs. A high-voltage static or sinusoidal potential is applied to the high-voltage electrode, and the other electrode is grounded.

3.2. Imaging system

The imaging system and experimental setup are shown in Fig. 5. Particles were imaged using an epifluorescent microscope (Nikon TE300) and a 60× oil-immersion objective with a numerical aperture (NA) of 1.4 and an effective depth of field of 260 nm [25]. Illumination was provided by a 100-W mercury lamp spectrally filtered with a filter cube (XF23 Omega Optical, Inc. Brattleboro, Vermont) having peak absorption and emission wavelengths of 485 and 535 nm, respectively.

Images were captured using a cooled CCD camera (CoolSNAP fx, Roper Scientific, Inc., Trenton, NJ) having a 1300 × 1030 array of square pixels, each with 12-bit intensity resolution and a edge dimension 6.7 μm. A 0.6× demagnifying lens was inserted into the optical path between the CCD camera and microscope to enlarge the field of view. The measurement volume was therefore 242 × 192 μm with a depth of approximately 300 nm. LabVIEW was used to synchronize the image acquisition with the high-voltage equipment.

3.3. Experimental procedure and image data collection

For the AC measurements, 41 single-frame images of multiple particle pathlines (streaks) were captured. An ex-

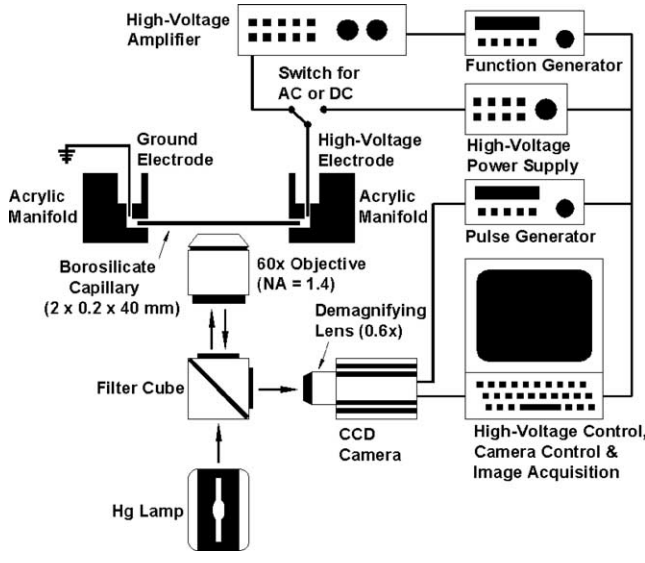

Fig. 5. Schematic of the experimental setup. Particles were imaged using an inverted, epifluorescent microscope fitted with a high-resolution CCD camera. For the DC measurements a high-voltage power supply provides a static potential to the high-voltage electrode. A function generator coupled to a high-voltage amplifier provides a sinusoidally varying potential for the AC measurements.

ample image is shown in Fig. 6a. In order to increase the signal-to-noise ratio of the particle streak images, the exposure time was set to two times (66 ms) the oscillation period (1/30 s) of the applied field. Images of particle streaks were captured at the centerline ($\tilde{y} = \tilde{z} = 0.5$) of the capillary to ensure maximum inertial decoupling of the wall slip velocity with the local fluid velocity. For a 30-Hz excitation, the penetration depth was $\delta = 103$ μm, resulting in $\beta = 1.94$ for $d = 200$ μm. For this β, $|\hat{u}(\tilde{z})| = 0.79$ and $\gamma(\tilde{z}) = -47.5°$ at $\tilde{z} = 0.5$.

Between successive images, 2 μl of seeded solution was introduced to advect new particles into the measurement volume. This procedure ensured that each particle streak was sampled only once, resulting in unbiased particle displacement data. A peak-to-peak voltage of 1000 V resulted in a mean streak length of roughly 15 particle diameters, thereby providing easily identifiable streaks.

The DC displacement distribution was measured by capturing 32 sequential particle images with an exposure time of 10 ms and a time spacing between frames of $\Delta t = 100$ ms. Individual particles were sampled only once (see flushing procedure above). Particle images were collected 5 μm above the surface of the capillary to ensure that particle displacements had a negligible pressure-driven-flow component (e.g., due to slight, unwanted differences between reservoir fluid levels). In both the AC and DC measurements, the electric field was only applied in 3 second bursts to minimize Joule heating, with image capture occurring 1 second after the application of the electric field. The 1 second time delay ensured that particle displacements were measured in a fully developed electroosmotic velocity field.

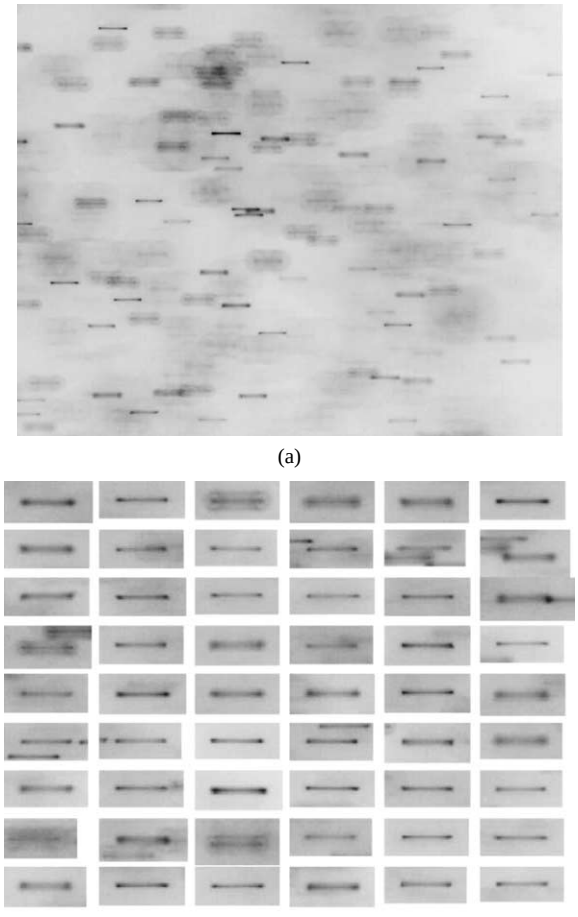

(a)

(b)

Fig. 6. AC particle streak images. Dark streaks represent oscillating particles in the inverted image intensity scale used here. (a) Typical image of raw AC particle displacement image data showing particles oscillating in deionized water. The camera exposure time was two times the period of the applied sinusoidal voltage. Blurred features represent out of focus particle streaks. (b) Streaks identified using a custom AC streak processing algorithm. This collection of streaks represents output from three images.

4. Image analysis

4.1. AC image processing

The AC image data were batch processed using a custom image processing algorithm written in MATLAB. Figure 6a shows a typical sample of the raw image data and Fig. 6b shows a collection of streaks identified and analyzed by the image processing algorithm. Each particle streak resembles a short line segment with two relatively bright "peaks" at each end. The flowchart shown in Fig. 7a illustrates the major image processing steps involved in automating the extraction of the particle streak lengths from the raw streak data. In order to remove high-spatial-frequency image noise, the raw image was first low-pass filtered using a Wiener filter. The image was then thresholded, keeping intensities above an empirically determined value that exceeded the in-

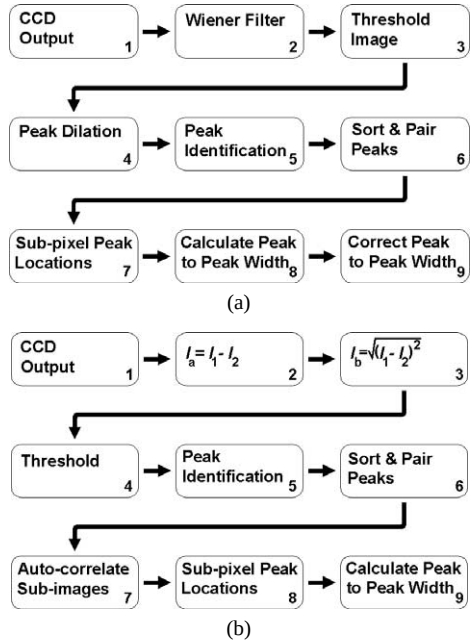

Fig. 7. Flowcharts showing AC and DC image processing steps. (a) The AC streak identification and extraction algorithm consists of nine steps and is used to determine particle displacement from streak images from the AC experiments. (b) The particle tracking algorithm used in DC image processing.

tensity of the region between peaks, yet did not surpass the intensity of the peaks. Thresholding produced a binary image, on which morphological operations were performed to remove stray outliers (i.e., isolated pixels with a value of unity). After the number of stray outliers was minimized, the resulting peaked regions were then dilated by convolving the entire binary particle streak image with the kernel

$$\begin{bmatrix} 0 & 1 & 0 \\ 1 & 1 & 1 \\ 0 & 1 & 0 \end{bmatrix}. \tag{34}$$

Convolution with this kernel smoothed the peaked regions, effectively removing any remaining isolated pixels resulting from image noise. The peaks were then labeled and sorted along pixel rows, as the streaks were predominantly oriented along the horizontal. Streaks were identified by searching for neighboring peaks in a user-defined subregion around each peak. For the data shown in Fig. 6b, the subregion ranged from ± 8 to ± 14 μm in the horizontal direction and ± 1.0 μm in the vertical direction from each identified peak. Possible candidates were validated through a "bridge check." If the intensity of the region midway between the peak and the possible candidate pair partner was significantly above the background noise level, then the peaks were assumed to form the ends of a streak and paired. Last, the peak-to-peak width of each streak was found by first searching for the location of maximum intensity of each peak. Subpixel resolution for the peak location was attained by fitting a two-dimensional Gaussian surface to the original image data in a 4×4 pixel region around the peak [26]. The streak length was defined as simply the distance between points of highest intensity of each dual-peak pair. Last, the AC particle displacement was determined from the streak length as described in the following section.

4.2. Simulated AC streak

An AC particle streak may be mathematically modeled as an Airy disk $a(r)$ convolved with a sinusoidally oscillating delta function $\delta(r(t))$,

$$g(r) = \int_0^T a(r)^{**}\delta\big(r(t)\big)\,dt, \tag{35}$$

where the "**" operator denotes a two-dimensional convolution. Since the spatial intensity recorded by the CCD camera is a time integration, the moving/oscillating Airy disk is integrated for the duration of the camera exposure time. The appropriate Airy disk is given by the convolution of the normalized impulse response with the brightness distribution of the particle,

$$a(r) = \left[\frac{2J_1\left(\frac{2\pi NA}{\lambda}r\right)}{\frac{2\pi NA}{\lambda}r}\right]^2 {}^{**}\mathrm{rect}\left(\frac{r}{2a}\right). \tag{36}$$

The first term represents the impulse response of a point source viewed through a circular aperture (i.e., microscope objective) as given by Fraunhofer diffraction theory [27]. J_1 represents the Bessel function of the first kind of order one, λ the wavelength of the emitted light, a the particle radius, and r the radial coordinate. The second term of the right-hand side of Eq. (36) represents the brightness pattern of the ideal particle image. The top-hat function $\mathrm{rect}(r)$ is defined as 1 for $|r| \leqslant 1/2$ and 0 for $|r| > 1/2$.

As a convenience, the Airy disk function can be approximated with a two-dimensional Gaussian function of the form

$$a(r) \approx \exp\left(-\frac{r^2}{\sigma^2}\right), \tag{37}$$

where σ^2 is the variance. With this approximation, the simulated streak function given in Eq. (35) may be expressed in Cartesian coordinates as

$$g(x,y) \approx \int_0^T \exp\left[-\frac{(x^2+y^2)}{\sigma^2}\right]^{**} \delta\left(x - \frac{d_{\mathrm{AC}}}{2}\cos(\theta)\cos(\omega t), y - \frac{d_{\mathrm{AC}}}{2}\sin(\theta)\cos(\omega t)\right) dt. \tag{38}$$

Here d_{AC} represents the peak-to-peak oscillation amplitude and θ denotes the angle of the particle trajectory with respect to the horizontal (i.e., the x-axis). An experimentally obtained intensity profile from raw data and a simulation of the expected intensity profile as given by Eq. (38) are shown in Fig. 8. Good qualitative agreement between the simulated streak and the raw data is observed.

This model illustrates an important difference between the true oscillation amplitude d_{AC} and the measured peak-to-peak width (i.e., the streak length) d_{meas}. Although the particle translates every half cycle, the streak length d_{meas} of the intensity profile is less than the true peak-to-peak amplitude. As the particle translates a distance d_{AC} in its sinusoidal trajectory, the majority of the particle's travel time is spent near the apex of the trajectory where the particle must first come to a halt before reversing direction. However, because the particle image has a finite diameter, the maximum integrated intensity occurs just inside of the apex. A 1-D plot of integrated particle image intensity of three particle image diameters and equal displacements d_{AC} is shown in Fig. 9a.

Equation (38) may be used to determine the relationship between the measured streak length and the true streak length. To this end, it is helpful to recast Eq. (38) in nondimensional form as

$$g(\tilde{x},\tilde{y}) \approx \frac{1}{\omega}\int_0^{2\pi} \exp\left[-\left(\tilde{x}^2+\tilde{y}^2\right)\right]^{**} \delta\left(\tilde{x} - \frac{\tilde{d}_{\mathrm{AC}}}{2}\cos(\theta)\cos(\tilde{t}), \tilde{y} - \frac{\tilde{d}_{\mathrm{AC}}}{2}\sin(\theta)\cos(\tilde{t})\right) d\tilde{t}, \tag{39}$$

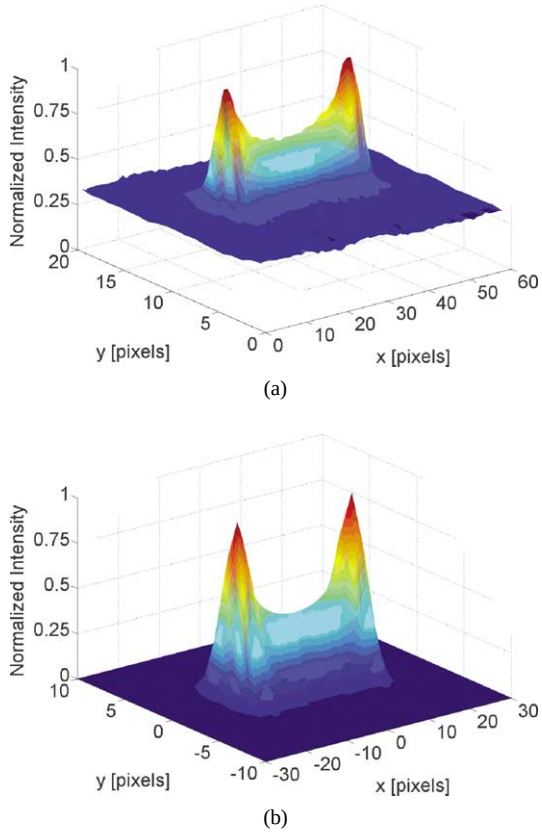

Fig. 8. Streak intensity profiles. Surface plots of a sample measured streak intensity field normalized by the maximum intensity (a) and a simulated streak profile constructed using a sinusoidal oscillating Gaussian function (b).

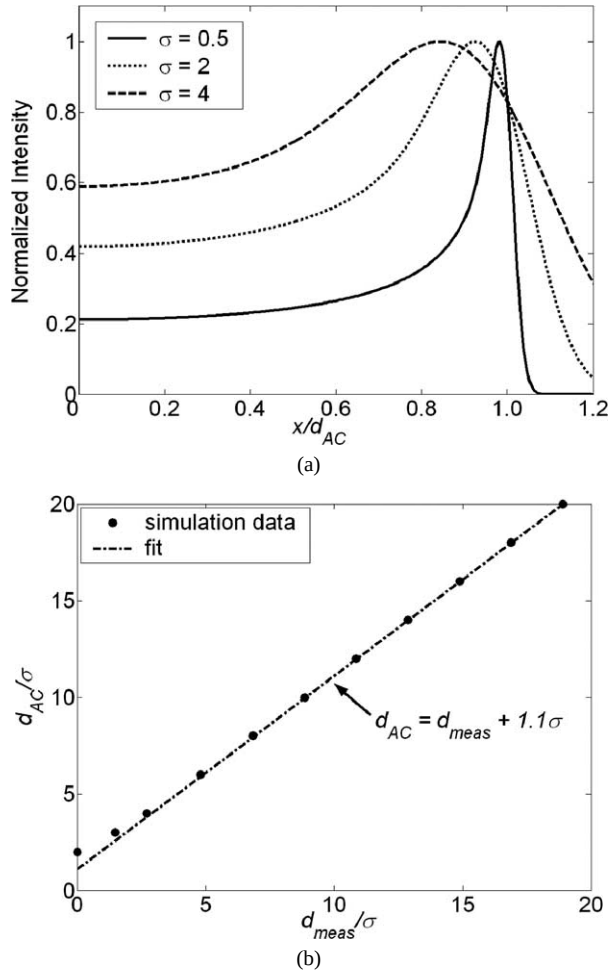

Fig. 9. (a) 1-D simulation of particle streak shown for various σ with displacement non-dimensionalized by d_{AC}. Since the particle streak is symmetric, only half of the particle trajectory is shown here for clarity. For σ tending to zero, the measured peak-to-peak width, defined as the distance between points of maximum intensity converges to d_{AC}. For σ increasing the measured peak-to-peak width decreases, resulting in a larger difference between d_{AC} and d_{meas}. The streak simulation provides the relationship between the d_{AC} and d_{meas}, shown in (b). A linear fit agrees with the simulation data to within 10% for $d_{\mathrm{meas}} \geqslant 2\sigma$.

where the spatial variables and time have been nondimensionalized by σ and ω, respectively. $g(\tilde{x}, \tilde{y})$ may be plotted for various values of $\tilde{d}_{\mathrm{AC}}$, showing that the observed peak-to-peak width $\tilde{d}_{\mathrm{meas}}$ varies with d_{AC} and σ as

$$d_{\mathrm{AC}} \approx 1.1\sigma + d_{\mathrm{meas}}. \tag{40}$$

This simple relationship holds to within 10% for $\sigma \leqslant d_{\mathrm{meas}}/2$, as shown in Fig. 9b. Note that Eq. (39) indicates that the measured peak-to-peak width is independent of the integration time, provided that the integration time is at least a half period of the excitation frequency.

4.3. DC image processing

A custom particle tracking velocimetry code written in MATLAB was used to interrogate the approximately one-dimensional DC displacements of 1000 particles in 32 images. The algorithm for particle pairing/tracking consisted of nine major steps, as shown in Fig. 7b. Starting with the second image in a sequence of images separated by $\Delta t = 100$ ms, each image was subtracted from the previous image in the sequence. This procedure subtracted unwanted background noise and resulted in images I_a having positive intensities associated with particles in the first image, I_1, and negative intensities from particles in a second image, I_2. To create only positive intensities, the images I_a were squared. The pixel intensities were rescaled by calculating the positive square root after the squaring operation. Peaks were identified using a thresholding procedure. Peaks were then paired by searching in a predefined subregion of ± 3 to ± 8 μm in the horizontal direction and ± 1.0 μm in the vertical direction from each identified peak. Subimages around each identified peak pair were than autocorrelated in Fourier space. The peak-to-peak displacement between the extreme (i.e., nonzero displacement) peaks of the three-peak autocorrelation corresponds to twice the particle displacement. The DC displacement was then measured with subpixel resolution using the subpixel peak estimator described above for the AC streak processing algorithm.

5. Results

Probability density functions of the measured AC and DC mobilities are shown in Fig. 10. The mean and standard deviation of μ_{AC} were 4.71 and 0.28 μm cm/V s, while μ_{DC} had a mean and standard deviation of 4.21 and 0.37 μm cm/V s, respectively. For the AC displacement measurements, the sample size or number of identifiable streaks was limited to 1000, resulting in an uncertainty in the mean of 0.02 μm cm/V s with 95% confidence. For the DC measurements, a sample size of 1000 yielded a corresponding uncertainty in the mean of 0.03 μm cm/V s.

Figure 11 displays PDFs of the electrophoretic and electroosmotic mobility estimates. The mean electrophoretic mobility was −3.76 μm cm/V s with a standard deviation of 0.73 μm cm/V s. For the electroosmotic mobility, the mean and standard deviation of the estimated mobility distribution was 7.94 and 0.69 μm cm/V s, respectively. For a mean electroosmotic mobility value of 7.94 μm cm/V s, the Helmholtz–Smoluchowski [2] relation for the mobility predicts a zeta potential of −115 mV. This value is within the range of published values of glass/deionized water interfaces. For example, Schwer and Kenndler [28] measured the electroosmotic velocity of a neutrally charged tracer in a fused-silica capillary using deionized water as the background electrolyte. For a pH of 7, they report an electroosmotic velocity of 1.75 mm/s, which using the Helmholtz–Smoluchowski relation equates to a zeta potential value of −121 mV for their electric field strength. As expected, the variation in the electroosmotic mobility is very small and due only to measurement error, an equal, uniform value for both the AC and DC experiments.

The application of Helmholtz–Smoluchowski theory to predict the mean zeta potential of the particles using the electrophoretic mobility is incorrect for these experiments, since the (quasi-static) electric double layer/particle system is predicted to be significantly polarized. The extent of double layer/particle system polarization may be characterized by the Dukhin number, which is a ratio of the surface conductivity of the particle to the fluid's bulk conductivity multiplied by the particle radius [19]. For Dukhin numbers of order unity or higher, the electric double layer/particle system is significantly polarized [15]. For the experiments considered

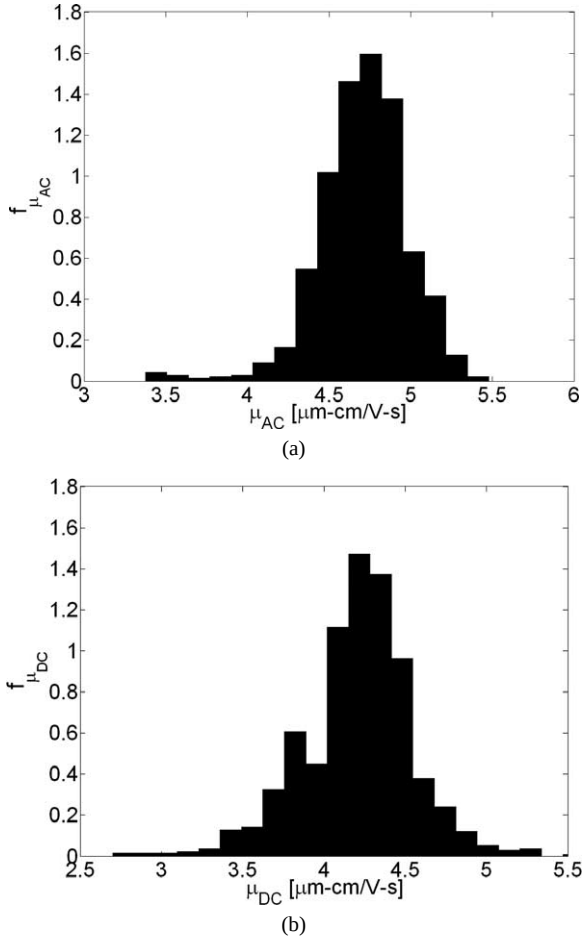

Fig. 10. Probability density functions of the observed AC and DC mobilities. (a) PDF of the AC field mobility, μ_{AC}, and (b) PDF of the DC field mobility, μ_{DC}.

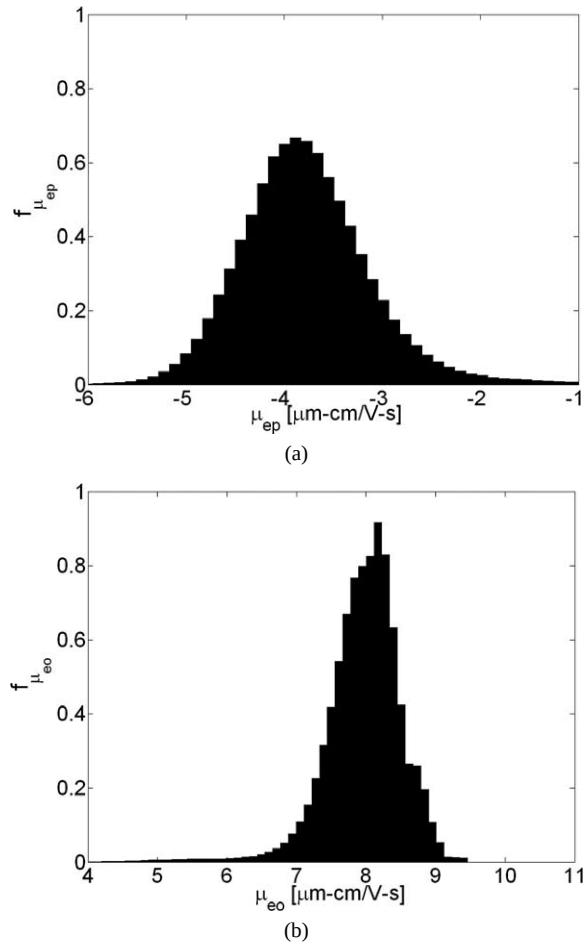

Fig. 11. Probability density functions of the electrophoretic and electroosmotic mobility estimate distributions. (a) PDF of μ_{ep}. The measured mean and standard deviation were −3.76 and 0.73 μm cm/V s. (b) PDF of μ_{eo} having a mean and deviation of 7.94 and 0.69 μm cm/V s.

here, the Dukhin number, *Du*, is estimated to be $O(1)$ assuming negligible conduction beneath the shear plane (i.e., within the particle's Stern layer). Any analysis that relates the particle mobility data reported here to particle zeta potential should, therefore, incorporate polarization effects. The reader is referred to the Dukhin–Seminikhin theory, described by Lyklema [19], which is valid for low nondimensional frequencies $\omega\tau \ll 1$, where $\tau = a^2/2D$, and takes into account polarization in the prediction of particle zeta potential from electrophoretic mobility.

6. Practical considerations

This section is offered as practical advice to experimentalists wishing to use this technique. In order to sufficiently decouple the wall velocity from the local fluid velocity along the capillary centerline, we recommend that the capillary dimension and frequency be chosen such that $\beta \geqslant 2$. However, the frequency should not be raised to arbitrarily high values to satisfy this condition, since the particle displacement is inversely proportional to the frequency. The absolute value of particle displacement and the diffraction-limited capabilities of the imaging system limit the degree of accuracy of the mobility measurements. The frequency should therefore be limited to a level such that the peak-to-peak width of the particle streaks represents about 10 particle widths. This ensures that particle streaks are readily discernible. Naturally, the electric field strength could also be increased to achieve larger peak-to-peak widths; however, the power density of Joule heating increases with the square of the electric field strength [29], and excessive Joule heating can result in undesirable temperature gradients and complex fluid flows leading to erroneous mobility measurements. In order to reduce Joule heating, buffers with low electrical conductivity should be used. For the electric field strength and deionized water used in this study, Joule heating resulted in less than 1 °C of temperature rise in the bulk fluid. In general, there is a direct tradeoff between the accuracy of the measurement (as determined by the displacement distance of particles, particle image diameter, and image resolution) and the conductivity of the solution (which limits the maximum allowable electric field to avoid undue temperature gradients).

7. Conclusions

Accurate measurement of the electrophoretic mobility of particles in liquid suspensions and the electroosmotic mobility of microchannel surfaces is crucial to understanding the stability of colloidal suspensions, obtaining particle-tracking-based velocimetry measurements of electroosmotic flow fields, and the quantification of electrokinetic bioanalytical device performance. We have presented a new, hybrid microelectrophoresis method for determining the distribution in electrophoretic mobility of submicrometer particles and the estimating electroosmotic mobility of a microchannel test cell. Independent measurements of particle displacements subjected to AC and DC electric fields are obtained using a high-resolution CCD camera. DC particle displacements were measured using a super-resolution PTV code. Full characterization of AC particle displacement requires a solution to the equations of fluid motion. We provide the periodic, steady-state solution for oscillatory electroosmotic flow resulting from an externally applied alternating electric field to a 2-D microchannel having azimuthal variation in electroosmotic mobility. Explicit expressions for μ_{ep} and μ_{eo} were derived as a function of AC and DC particle displacements. A statistical analysis was presented that can be used to calculate distributions of the estimates of μ_{ep} and μ_{eo} given measured particle displacement distributions.

A custom image-processing algorithm enabled the quantification of the peak-to-peak width of 1000 individual particle streaks using a subpixel-accurate scheme. A model of the imaged particle streak using analytical convolution expressions shows that the peak-to-peak width underestimates the true peak-to-peak oscillation amplitude of the particle for finite particle image diameters. A method for determining true particle displacements given streak image measurements was formulated.

The mean electrophoretic mobility of the 500 nm diameter polystyrene particles doped with a fluorescent dye with peak excitation and emission wavelengths of 490 and 515 nm, respectively was found to be -3.76 ± 0.05 μm cm/V s, while the mean electroosmotic mobility of the glass microchannel was 7.94 ± 0.04 μm cm/V s, for 95% confidence intervals. This value for the electroosmotic mobility implies a zeta potential for the glass surface of -115 ± 10 mV, which agrees well with the previously published values for glass/water interfaces at pH 7.

Acknowledgments

This work was sponsored by DARPA Contract F30602-00-2-0609 with Dr. Anantha Krishnan as contract monitor. M.H.O. is supported by a Department of Defense National Defense Science and Engineering Graduate (NDSEG) Fellowship.

Appendix A

The 2-D solution to the fluid equations of motion given in Eq. (2) subject to the boundary conditions given by Eq. (4) can be found by assuming a solution of the form $u = u(y,z,t) = f(y)g(z)\exp(i\omega t)$ and expanding the appropriate eigenfunctions. The solution for the steady, time-periodic, electroosmotic velocity profile is

$$u_{\mathrm{eo,AC}}(\tilde{y},\tilde{z},\tilde{t}) = \mathrm{Re}\left\{\sum_{n=1}^{\infty}\begin{pmatrix} A_n \sin(\chi_n d\tilde{y})\sinh(\varphi_n w\tilde{z}) \\ + B_n \sin(\chi_n d\tilde{y})\big[\sinh(\varphi_n w\tilde{z}) \\ \quad - \tanh(\varphi_n d)\cosh(\varphi_n d\tilde{z})\big] \\ + C_n \sin(\xi_n w\tilde{z})\sinh(\psi_n d\tilde{y}) \\ + D_n \sin(\xi_n w\tilde{z})\big[\sinh(\psi_n d\tilde{y}) \\ \quad - \tanh(\psi_n w)\cosh(\psi_n w\tilde{y})\big] \end{pmatrix}\exp(i\tilde{t})\right\}, \tag{A.1}$$

where Re represents the real part. The spanwise coordinate, transverse coordinate, and time have been nondimensionalized as $\tilde{y} = y/w$, $\tilde{z} = z/d$, and $\tilde{t} = \omega t$, respectively. The eigenvalues are

$$\chi_n = \frac{n\pi}{d},$$
$$\varphi_n = \frac{\sqrt{\chi_n^2 + 2i\beta^2 r^2}}{rd},$$
$$\xi_n = \frac{n\pi}{w},$$
$$\psi_n = \frac{r\sqrt{\xi_n^2 + 2i\beta^2}}{w}, \tag{A.2}$$

where the penetration depth, penetration ratio, and channel aspect ratio are $\delta = (2\nu/\omega)^{0.5}$, $\beta = d/\delta$, and $r = w/d$, respectively. i is the unit imaginary number. The Fourier coefficients are

$$A_n = \frac{2U_{\mathrm{slip},1}}{n\pi\sinh(\varphi_n d)}\big[1-\cos(\chi_n w)\big],$$
$$B_n = \frac{2U_{\mathrm{slip},2}}{n\pi\tanh(\varphi_n d)}\big[\cos(\chi_n w)-1\big],$$
$$C_n = \frac{2U_{\mathrm{slip},3}}{n\pi\sinh(\psi_n w)}\big[1-\cos(\xi_n d)\big],$$
$$D_n = \frac{2U_{\mathrm{slip},4}}{n\pi\tanh(\psi_n w)}\big[\cos(\xi_n d)-1\big]. \tag{A.3}$$

References

[1] J.P. Landers (Ed.), Handbook of Capillary Electrophoresis, CRC Press, Boca Raton, FL, 1997.

[2] R.J. Hunter, Zeta Potential in Colloid Science, Academic Press, London, 1981.

[3] J.Th.G. Overbeek, Electrokinetic Phenomena, Elsevier, New York, 1952.

[4] S. Devasenathipathy, J.G. Santiago, Anal. Chem. 74 (2002) 3704–3713.

[5] E.B. Cummings, Exp. Fluids 29 (2000) S42–S50.

[6] R.P. Sawatzky, A.J. Babchin, J. Fluid Mech. 246 (1993) 321–334.

[7] B.R. Ware, Adv. Colloid Interface Sci. 4 (1974) 1–44.

[8] E. Delatour, M. Hanss, Rev. Sci. Instrum. 47 (1976) 1531–1535.

[9] L.D. Sher, H.P. Schwan, Science 148 (1965) 229–231.

[10] G.V.F. Seaman, R.J. Knox, Electrophoresis 22 (2001) 373–385.

[11] S. Komagata, Res. Electrotechn. Lab. Jpn. 348 (1933) 5.

[12] D.R. Reyes, D. Iossifidis, P.A. Auroux, A. Manz, Anal. Chem. 74 (2002) 2623–2636.

[13] D. Erickson, D.Q. Li, J. Colloid Interface Sci. 237 (2001) 283–289.

[14] X. Huang, M.J. Gordon, R.N. Zare, Anal. Chem. 60 (1988) 1837–1838.

[15] M. Minor, A.J. van der Linde, H.P. van Leeuwen, J. Lyklema, J. Colloid Interface Sci. 189 (1997) 370–375.

[16] J.J. Lopez-Garcia, J. Horno, F. Gonzalez-Caballero, C. Grosse, A.V. Delgado, J. Colloid Interface Sci. 228 (2000) 95–104.

[17] V.N. Shilov, A.V. Delgado, F. Gonzalez-Caballero, J. Horno, J.J. Lopez-Garcia, C. Grosse, J. Colloid Interface Sci. 232 (2000) 141–148.

[18] N.G. Green, A. Ramos, H. Morgan, J. Phys. D Appl. Phys. 33 (2000) 632–641.

[19] J. Lyklema, Fundamentals of Interface and Colloid Science, in: Solid–Liquid Interfaces, Vol. II, Academic Press, London, 1995.

[20] R.F. Probstein, Physicochemical Hydrodynamics, 2nd ed., Wiley, New York, 1994.

[21] M.H. Oddy, J.G. Santiago, Anal. Chem. 73 (2001) 5822–5832.

[22] J.G. Santiago, Anal. Chem. 73 (2001) 2353–2365.

[23] P.G. Righetti, Capillary Electrophoresis in Analytical Biotechnology, CRC Press, Boca Raton, FL, 1996.

[24] S. Devasenathipathy, J.G. Santiago, Micro- and Nano-Scale Diagnostic Techniques, Springer-Verlag, New York, 2003.

[25] S. Inoue, K. Spring, Video Microscopy: The Fundamentals, Plenum, New York, 1997.

[26] M. Raffel, C.E. Willert, J.K. Willert, Particle Image Velocimetry: A Practical Guide, Springer-Verlag, New York, 1998.

[27] E. Hecht, Optics, Addison–Wesley, Reading, MA, 2002.

[28] C. Schwer, E. Kenndler, Anal. Chem. 63 (2001) 1801–1807.

[29] A. Ramos, H. Morgan, N.G. Green, A. Castellanos, J. Phys. D Appl. Phys. 31 (1998) 2338–2353.